Optics Letters

On-chip reconfigurable polarization splitter-rotator fabricated on a thin-film lithium niobate photonic integrated circuit platform

FLORIAN DUBOIS,* ALBERTO DELLA TORRE, JACOPO LEO, DORIAN HERLE, ARNO METTRAUX, HOMA ZAREBIDAKI, HAMED SATTARI, AND MICHEL DESPONT

Swiss Center for Electronics and Microtechnology (CSEM), Neuchatel, Switzerland
**florian.dubois@csem.ch*

Received 8 October 2025; revised 9 December 2025; accepted 11 December 2025; posted 11 December 2025; published 23 December 2025

We report the conception and experimental demonstration of a tunable polarization splitter-rotator (PSR) integrated into a thin-film lithium niobate (TFLN) photonic platform based on a 45° PSR. The device operates over the C-band and leverages the thermo-optical tunability of TFLN to achieve precise and stable manipulation of the polarization in a millimeter scale footprint. The PSR exhibits a polarization extinction ratio of 23.3 dB on average near 1550 nm, enabling separation of both polarization channels. This performance highlights the potential of TFLN for dual-polarization applications in optical communications, sensing, and beyond.

https://doi.org/10.1364/OL.580756

Introduction. Polarization management is a fundamental function in photonic integrated circuits (PICs), enabling key capabilities in coherent optical communications, and polarization-diverse signal processing. Polarization management in PICs involves different components such as polarization rotator which converts orthogonal polarization modes, typically the fundamental quasi-transverse electric (TE0) and quasi-transverse magnetic (TM0) modes, into one another with high polarization conversion efficiency (PCE) [1,2]. Polarization beam splitters split the intensity in each polarization mode into two spatially separated channels while preserving the initial polarization of the mode [3,4]. Finally, polarization splitter-rotators (PSR) plays a central role among polarization management components, enabling the spatial separation of the polarization mode into identically polarized channels, mitigating the need of polarization-insensitive components as both channels are independently processed in the same polarization mode, which is particularly interesting for dual-polarization transceivers [5]. Recent advances in silicon photonics have also demonstrated that leveraging hybrid mode bases, such as linear combinations of TE0 and TM0 instead of pure TE0 and TM0 base, to generate so-called 45° PSR, can enable the design of more optimal devices without compromising on the usability for certain applications such as optical receivers [6].

In this work, we extend this design paradigm to the thin-film lithium niobate (TFLN) platform, which offers a compelling combination of low optical loss, high electro-optic coefficients, high-speed modulation capability and low-power consumption capability [7–10]. We present a tunable PSR operating at the telecom wavelengths, achieving polarization extinction ratios (PER) of 23.3 dB on average. The device architecture integrates a tapered mode converter and a symmetric Y-splitter for the 45° PSR encompassed in a Mach–Zehnder Interferometer (MZI) circuit, enabling efficient rotation and separation of polarization modes with minimal insertion loss and polarization-dependent loss (PDL). The MZI is integrated with thermo-optically tunable phase shifters (TO-PS). This configuration allows post-fabrication-tuning of the output phase and mode separation [11], restoring optimal PSR functionality while leveraging the stability and compactness of TFLN TO-PS [12].

The proposed PSR is implemented using the CSEM-TFLN-3WG2MET technology. Comprehensive simulations based on the platform manufacturability criteria are used to optimize each component and infer the performance of the PSR. Finally, experimental measurements are performed to assess the passive performance and tunability of the fabricated PSR.

While passive PSRs have been explored on TFLN [13–15], and thermo-optic tuning is a well-known technique, this work, for the first time to our knowledge, integrates the 45° PSR concepts to demonstrate a fully reconfigurable PSR on a 150-mm foundry-compatible TFLN platform. This step is critical for demonstrating a practical path toward scalable manufacturing of advanced, dual-polarization photonic integrated circuits that can actively compensate for inevitable fabrication variations.

Device concept and working principle. A polarization splitter-rotator is a device with one or two inputs and two outputs, designed to convert and separate the fundamental quasi-TE and quasi-TM modes of a waveguide or input fiber. It outputs two spatially separated waveguides carrying identically polarized modes, enabling independent signal processing. Assuming the target output polarization is TE, the TE0 mode is directed into one branch, while the TM0 mode is converted into TE0 and routed into the other branch. The working operation is depicted in Fig. 1(a).

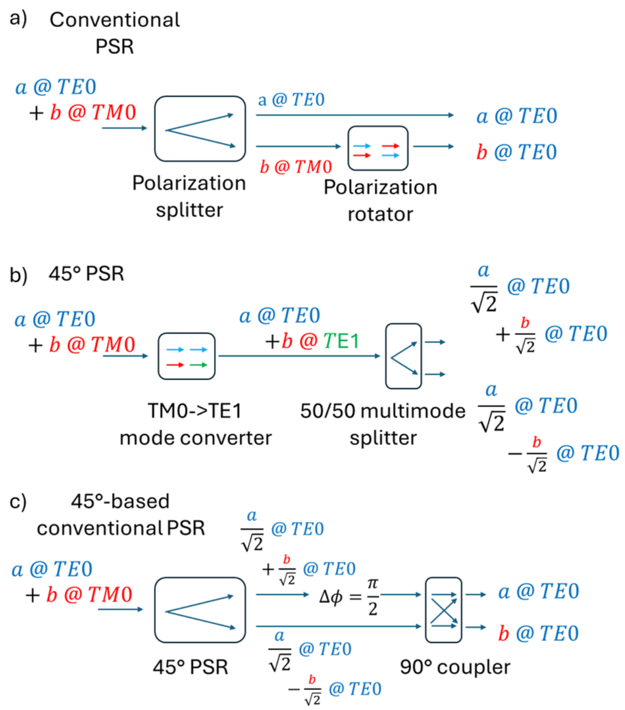

Fig. 1. (a) Working operation of a PSR, illustrated using a polarization beam splitter followed by a polarization rotator. (b) Working operation of a 45° PSR. (c) Working operation of a PSR based on a 45° PSR. Blue (resp. red) refers to TE (resp. TM) polarization and input power a (resp. b).

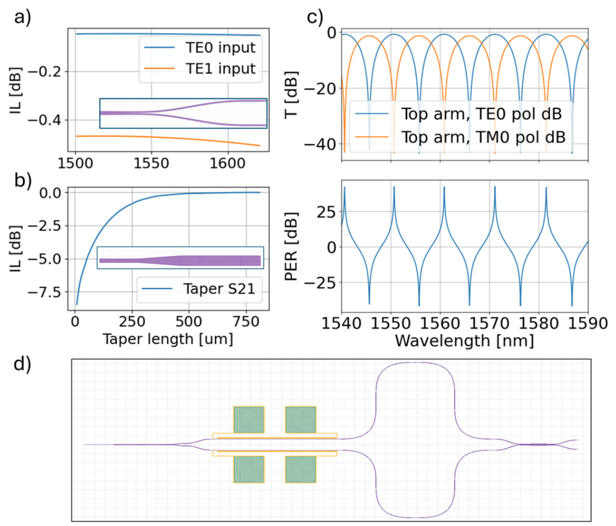

Fig. 2. (a) Power loss simulation results of the TM0-TE1 mode converter at 1550 nm and (b) of the Y-splitter forming the 45° PSR for TE0 and TE1 input over the C- and L-bands. (c) Circuit simulation of the PSR depicting the transmission spectrum for TE0 and TM0 inputs in dB (top) and the derived PER in dB (bottom) and (d) GDS layout if the PSR circuit.

The effectiveness of polarization separation is evaluated using the PER, defined as the ratio of TE to TM transmission in dB. Additionally, minimizing insertion loss (IL) for both TE0 and TM0 inputs is crucial as well as reducing polarization-dependent loss (PDL).

To address this issue, we propose a tunable PSR architecture based on a 45° PSR integrated within a thermo-optically tunable MZI. This configuration enables controlled mode separation at the output of the MZI to restore the PSR functionality and allows fine-tuning for optimal performance. The proposed architecture is depicted in Fig. 1(c).

The 45° PSR operation, depicted in Fig. 1(b), comprises two main parts: (1) a tapered section that adiabatically converts the TM0 mode into TE1, while leaving the TE0 mode unaffected, and (2) a symmetrically designed Y-splitter, optimized for equal (50/50) splitting of TE0 and TE1 modes with minimal insertion loss.

The outputs of the 45° PSR feed into a Mach–Zehnder interferometer equipped with thermo-optic phase shifters (TO-PS) on each arm, enabling tunability. For simplified characterization and demonstration, an asymmetric MZI is used in this Letter, where the required phase shift is achieved by tuning the measurement wavelength, allowing the PSR to also operate passively. A practical PSR device would however be designed with a balanced MZI and rely solely on the TO-PS to perform the phase tuning, which would exhibit a much broader and flatter response. A 2 × 2 multimode interferometer (MMI) optimized for TE0 polarization is used as 90° coupler to recombine the MZI arms.

This design approach, inspired by recent advances in silicon photonics [6], is adapted to the TFLN platform to leverage its low-loss properties, thereby reducing both insertion loss and PDL in the PSR, and low-power consumption capability.

Platform, design, and simulation. The PSR is implemented on CSEM's foundry compliant with the 150 mm wafer scale CSEM-TFLN-3WG2MET technology [16]. The fabrication technology is based on commercially available TFLN wafers consisting of a stack of 600 nm thick x-cut $LiNbO_3$ layer on top of a 4.7 µm buried oxide layer. The waveguides and PSR are fabricated by etching 400 nm of $LiNbO_3$ by dry etching, and a layer of metal is deposited to form the TO-PS electrodes and pads. The waveguides are cladded by a deposited silicon oxide layer which is selectively etched to open the metal pads.

The PSR design was optimized in multiple stages:

I. The adiabatic mode converter was designed using a finite-difference eigenmode (FDE) solver to determine the optimal taper width. A theoretical maximum PCE of 99% is achieved for a waveguide width of 2 µm in the Z-direction. The adiabatic taper length was determined using 3D eigenmode expansion method (EME) simulations from ANSYS Lumerical, yielding an insertion loss below 0.2 dB for a taper length of 400 µm at 1550 nm for a total PCE of 0.25 dB. The TE0 mode exhibits negligible IL. The simulation results are depicted in Fig. 2(a).

II. A Y-splitter was designed through 3D finite-difference time-domain (FDTD) simulations from ANSYS Lumerical. Insertion loss was minimized by refining the design within the design rules of the CSEM-TFLN-3WG2MET platform. As a result, insertion losses below 0.05 dB were achieved for TE0 and 0.5 dB for TE1 input modes as depicted in Fig. 2(b), enabling the PSR 45° functionality.

III. The 90° coupler is based on an MMI 2 × 2 and was optimized using 3D EME simulations from ANSYS Lumerical, resulting in a power imbalance of 0.13 dB and an IL of 0.7 dB at 1550 nm.

IV. The thermo-optic phase shifters (TO-PS) were designed using multi-physics simulations in COMSOL Multiphysics combining thermal and wave-optics models. A meander topol-

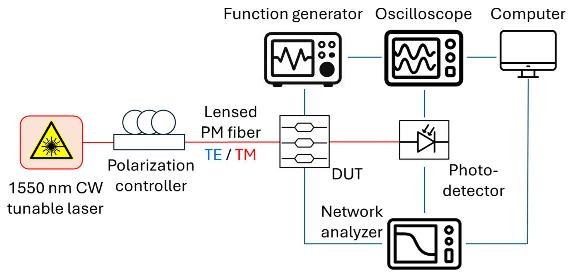

Fig. 3. Schematic of the characterization setup for passive and electrical characterizations.

ogy for the metal electrode has been designed to increase the efficiency of the TO-PS. To simplify the layout and the waveguide fan-out to the edge couplers, the TO-PS were placed along the Z-direction for these demonstrators. In this direction, the TO-PS is expected to be less power-efficient due to a lower thermo-optic coefficient compared to the Y-direction [17]. A practical implementation can combine the Z-direction tapers with Y-direction TO-PS and multiple pass of the waveguide to improve the power efficiency even further, power as low as 39.1 mW is demonstrated on a TFLN platform [18].

V. The overall PSR circuit behavior was simulated and validated using Sax. The simulation results are given in Fig. 2(c). The designed PSR exhibits a simulated polarization extinction ratio (PER) larger than 43 dB, limited by the power splitting imbalance of the splitter of the MZI. The simulated insertion loss is −1.05 dB for TE0 and −1.55 dB for TM0 inputs, with a major contribution arising from the MMI 2 × 2.

Finally, the layout of the PSR depicted in Fig. 2(d) was implemented on Nazca, it is depicted in Fig. 2(d). A PSR enabling direct measurement of its outputs using edge couplers is designed. It exhibits an MZI with a length imbalance of 100 μm and a TO-PS with a length of 600 μm.

Characterization methods and results. To characterize the designed PSR, an optical bench enabling transmission spectrum measurement and electrical tuning has been used. The schematics of the bench is provided in Fig. 3. To input pure TE0, we optimize the polarization-maintaining (PM) fiber angle to align on the vertical or horizontal axis of the chip by monitoring parasitic ripples on the spectrum of a reference waveguides on the chip. A coarse adjustment of the polarization input is first made by taking advantage of the PDL of the edge coupler, which exhibits larger losses for TM0 mode on the reference arm of the chip. By adjusting the polarization controller and maximizing the output signal of the photo-detector, we align the output polarization on the TE0 mode. A fine-tuning of the polarization is made using the outputs of the PSR, by increasing the extinction ratio of the IMB-MZI. The TM0 polarization is obtained in a similar fashion, by enabling the largest extinction ratio of the IMB-MZI at its out-of-phase location. The transmission spectrum of the reference arm and both PSR outputs are recorded for both TE0 and TM0 polarization inputs. Finally, the dark current of the photo-detector is recorded with the laser light turned off and subtracted from the transmission measurement to retrieve an accurate estimation of the PER.

Figure 4 depicts the transmission measurement results, normalized by the reference arm measurements, and post-processed PER on a wavelength region between 1540 and 1590 nm for the upper arm of a PSR with 200 μm MZI imbalance and 600 μm

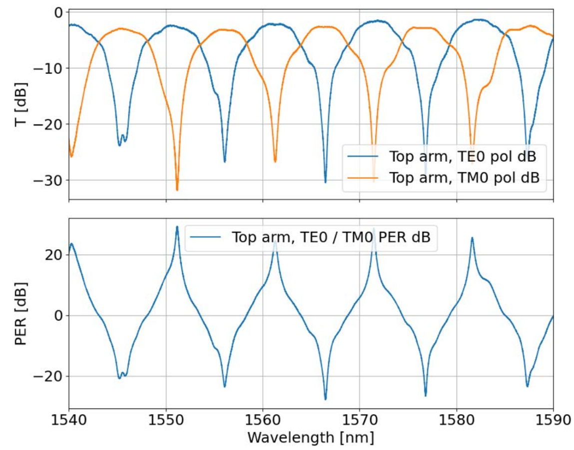

Fig. 4. Passive measurement results of the fabricated chip, from top to bottom, the transmission spectrum for TE0 and TM0 inputs in dB and the derived PER in dB.

long TO-PS. A PER of 23.3 ± 4 dB is reached for TE0 and TM0 polarization at the wavelengths where the MZI provides the proper $\pi/2$ phase shift. The drop of the PER compared to the simulation are attributed to a higher power imbalance in the MMI 2 × 2 and Y-Splitter, in particular for TM0 input for the latter, compared to the simulation. The IL of the PSR is 1.78 dB ± 0.51 dB for TE0 and 2.36 dB ± 0.47 dB for TM0 in the 1540 to 1590 nm range by monitoring the peak level of the normalized transmission in both arms. The deviation of the TM0 IL measurements compared to simulations is attributed to the reproducibility of the edge coupling between the reference and the PSR.

In order to assess these thermo-optic characteristics, we performed resistivity measurement of the TO-PS using an Agilent 4294 A Precision Impedance Analyzer. A pad-to-pad resistance of 358 Ω is measured. Then, active measurements are performed using a DS340 function generator from Stanford Research Systems. A 100 Hz, 3.5 V amplitude zero-centered triangular signal is generated. The wavelength of the laser is placed at the quadrature point of the MZI. The results are depicted in Fig. 5(a). Due to the breakdown voltage of the TO-PS, the V_π cannot be reached and is only extrapolated from lower values. Assuming the temperature coefficient of resistance can be neglected, a V_π of 14.7 V ± 0.3 V and a P_π of 600 mW ± 20 mW are extrapolated. The high power requirement is attributed to the direction of the TO-PS.

To measure the frequency response of the TO-PS, we use a network analyzer generating a sinusoidal wave for the excitation input with an amplitude of 1 V and a DC bias of 1 V. The frequency of the modulation input is swept from 100 Hz to 200 kHz. The results are depicted in Fig. 5(b). A 3 dB modulation bandwidth of 3.55 kHz is measured. The corresponding modulated signal in the time-domain at 100 Hz and 4 kHz from a 3.5 V zero-centered sinusoidal at modulated half the frequency, due to the V^2 dependency of the TO-PS modulation, is depicted in the insets.

To demonstrate the practical benefit of the device's reconfigurability, we actively tuned the TO-PS to optimize performance. As shown in Fig. 5(c), applying power to the heater directly compensates for phase errors in the MZI, resulting in a clear improvement in the measured PER. This confirms that the active

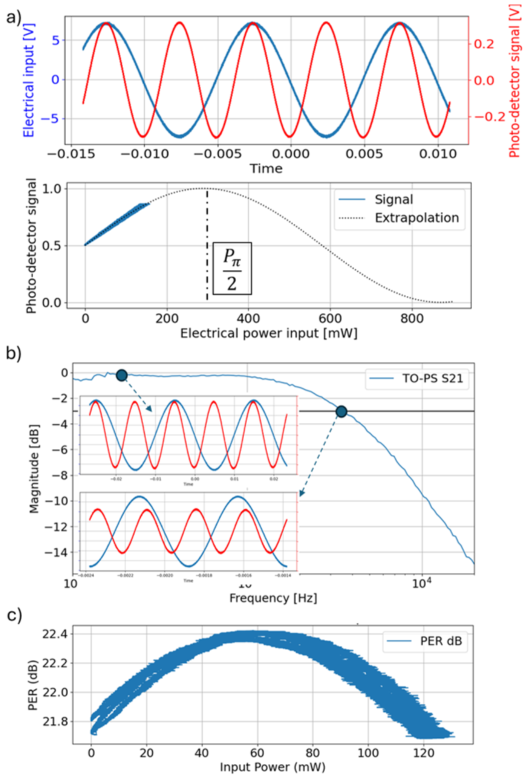

Fig. 5. (a) Thermal tuning of the PSR at the quadrature point with the electrical signal and AC-coupled photo-detector output (top) and the normalized photo-detector signal versus electrical power (bottom). (b) Frequency response of the PSR at the quadrature point, the insets are the time-domain signal at equivalent frequencies. (c) Demonstration of active PER tuning, showing improvement in the extinction ratio at 1550 nm as power is applied to the TO-PS.

Table 1. State-of-the-Art Comparison of PSRs

Platform	Reference	Per (dB)	IL (dB)	Tunable?
TFLN	[2]	>19	<1	No
TFLN	[19]	>12.2	<0.91	No
SiN	[20]	>30	<1	No
Si	[21]	>22	<2.3	Yes
TFLN	**This Work**	**23.3**	**<2.36**	**Yes**

tuning can be used to overcome fabrication-induced imbalances and achieve optimal device operation.

Discussion and conclusion. We proposed a design for a tunable PSR for the first time in our PDK-based TFLN photonic platform. The PSR allows for the separation of any TE0/TM0 combination from an input fiber and separates them into different channels in the same TE-polarization for independent processing. The demonstrated PSR manufactured following foundry-compatible technology rules exhibits PER of 23.3 dB and an IL lower than 2.36 dB near 1550 nm wavelength.

To contextualize these results, we compare our device's performance against the state-of-the-art for polarization splitter-rotators on various photonic platforms. Table 1 summarizes this comparison.

As shown in Table 1, our device achieves a PER that is comparable to that of other passive PSRs on the TFLN platform. Crucially, our work introduces active reconfigurability, a feature absent in prior TFLN demonstrations, which provides a demonstrated mechanism for post-fabrication performance optimization. This paves the way to large-scale integration of PSR on chip and precise control of polarization, enabling better performing PICs on the TFLN platform unlocking many functionalities from telecom to advanced sensing and navigation applications.

Funding. European Commission (101070506, 101070441, 101070581).

Disclosures. The authors declare no conflicts of interest.

Data availability. Data underlying the results presented in this paper are not publicly available at this time but may be obtained from the authors upon reasonable request.

REFERENCES

1. L. Chen, C. R. Doerr, and Y.-K. Chen, Opt. Lett. **36**, 469 (2011).
2. J. Wu, W. Liu, D. Dai, *et al.*, Opt. Lett. **50**, 5622 (2025).
3. Y. Xu, J. Xiao, and X. Sun, J. Lightwave Technol. **32**, 4282 (2014).
4. D. Dai and J. E. Bowers, Opt. Express **19**, 18614 (2011).
5. D. Dai and H. Wu, Opt. Lett. **41**, 2346 (2016).
6. Y. Ma, Y. Liu, H. Guan, *et al.*, Opt. Express **23**, 16052 (2015).
7. D. Zhu, L. Shao, M. Yu, *et al.*, Adv. Opt. Photon. **13**, 242 (2021).
8. C. Wang, M. Zhang, and X. Chen, Nature **562**, 101 (2018).
9. A. Della Torre, F. Dubois, H. Zarebidaki, *et al.*, Opt. Express **33**, 6747 (2025).
10. X. Zhu, M. M. de Freitas, S. Shi, *et al.*, IEEE J. Sel. Top. Quantum Electron. **30**, 1 (2024).
11. Z. Lin, Y. Lin, H. Li, *et al.*, Light. Sci. Appl. **11**, 93 (2022).
12. A. Maeder, F. Kaufmann, D. Pohl, *et al.*, Opt. Lett. **47**, 4375 (2022).
13. C. Li, G. Chen, Y. Huang, *et al.*, APL Photonics **10**, 016111 (2025).
14. X. Wang, A. Pan, T. Li, *et al.*, Opt. Express **29**, 38044 (2021).
15. J. Zhang, K. Zhou, X. Liu, *et al.*, J. Appl. Phys. **136**, 164503 (2024).
16. A. Della Torre, H. Zarebidaki, A. Mettraux, *et al.*, in Advanced Photonics Congress (IPR, Networks, NOMA, SOLITH, SPPCom) (Optica Publishing Group, 2025), p. ITu2A.1.
17. S. A. Hbeeb and A. S. Abdullah, J. Opt. **54**, 3684 (2025).
18. H. Ji, L. He, F. Yue, *et al.*, J. Light. Technol. **43**, 6833 (2025).
19. Y. Wu, X. Sun, X. Xue, *et al.*, J. Light. Technol. **42**, 2429 (2024).
20. Z. Mokeddem, E. Cassan, D. Marris-Morini, *et al.*, in *2024 IEEE Silicon Photonics Conference (SiPhotonics)* (2024). p. 1.
21. W. D. Sacher, T. Barwicz, B. J. F. Taylor, *et al.*, Opt. Express **22**, 3777 (2014).